Spin-induced dynamical scalarization, descalarization, and stealthness in scalar-Gauss-Bonnet gravity during a black hole coalescence

Matthew Elley,[1,*] Hector O. Silva,[2,†] Helvi Witek,[3,‡] and Nicolás Yunes[3,§]

[1]*Department of Physics, King's College London, Strand, London, WC2R 2LS, United Kingdom*
[2]*Max Planck Institute for Gravitational Physics (Albert Einstein Institute), Am Mühlenberg 1, D-14476 Potsdam, Germany*
[3]*Illinois Center for Advanced Studies of the Universe & Department of Physics, University of Illinois at Urbana-Champaign, Urbana, Illinois 61801, USA*

(Received 18 May 2022; accepted 11 July 2022; published 8 August 2022)

Particular couplings between a scalar field and the Gauss-Bonnet invariant lead to spontaneous scalarization of black holes. Here, we continue our work on simulating this phenomenon in the context of binary black hole systems. We consider a negative coupling for which the black-hole spin plays a major role in the scalarization process. We find two main phenomena: (i) dynamical descalarization, in which initially scalarized black holes form an unscalarized remnant, and (ii) dynamical scalarization, whereby the late merger of initially unscalarized black holes can cause scalar hair to grow. An important consequence of the latter case is that modifications to the gravitational waveform due to the scalar field may only occur postmerger, as its presence is hidden during the entirety of the inspiral. However, with a sufficiently strong coupling, we find that scalarization can occur before the remnant has even formed. We close with a discussion of observational implications for gravitational-wave tests of general relativity.

DOI: 10.1103/PhysRevD.106.044018

I. INTRODUCTION

The detection of gravitational waves (GW) produced by coalescing compact binaries by the LIGO-Virgo-Kagra Collaboration [1–3] have opened a new avenue to test general relativity (GR) in its strong-field, nonlinear regime [4–8]. In fact, the first three catalogs of observations have already been used to perform several null tests of GR [8–17], as well as theory-specific tests [18–26]. The latter have placed constraints on quadratic gravity theories [21–25].

In these theories, a scalar field couples to a curvature scalar, which is quadratic in the Riemann tensor (see, e.g., Ref. [27] for an overview). Well-known examples include coupling to the Pontryagin density or the Gauss-Bonnet (GB) invariant. The latter theories are often named scalar Gauss-Bonnet (sGB) gravity. They can emerge in the low-energy limit of string theory (see, for instance, Refs. [28–30]), as well as through a dimensional reduction of Lovelock gravity [31], and belong to the wider class of Horndeski gravity theories [32,33].

Black hole (BH) solutions in this theory have long been known to have a nontrivial scalar field (i.e., a "hair"), to which we can associate a monopole scalar charge that depends on the BH's mass and spin. When the BHs are found in a binary, their motion can lead to the emission of scalar dipole radiation, which in turn modifies the system's orbital dynamics and the GW signal with respect to GR's prediction. Such phenomenology has been explored with both post-Newtonian (PN) [34–40] and numerical relativity [41–46] techniques. The scalar field can also affect the post-merger signal, modifying the remnant BH's ringdown [47–52]. In sGB gravity, the presence of scalar hair depends on the functional form of the coupling between scalar field and the GB invariant.

More specifically, if the functional form of the coupling always has a nonvanishing first derivative, such as for a linear or exponential coupling, BHs are known to invariably have scalar hair [53–67]. Hence, the observation of GWs from BH binaries and mixed neutron star (NS)-BH binaries have allowed us to constrain the length scale at which the scalar-field-GB interaction becomes relevant to less than approximately one kilometer [22–25].

In contrast, if the first derivative of the coupling function vanishes for some constant background scalar field, both scalarized and unscalarized BH solutions can exist [68,69]. Depending on the length scale associated with the scalar-field-GB interaction, and the BH's mass [68–70] and spin [71–78], the BH solutions of GR become unstable to scalar field perturbations, and the end-state of this instability is a *scalarized* BH [79]. This process is similar to spontaneous scalarization of NSs in scalar-tensor gravity [80,81].

*matthew.elley@kcl.ac.uk
†hector.silva@aei.mpg.de
‡hwitek@illinois.edu
§nyunes@illinois.edu

The difference lies in the fact that for NSs the scalar field is sourced by matter, while for BHs the scalar is sourced by the spacetime curvature alone. Thus, one could envision that the aforementioned GW constraints (such as e.g., Ref. [21]) can be avoided if scalarization occurs *right before merger, or possibly only after merger.*

Can such a scenario happen? Here, we continue our previous work [45] and explore how the onset of scalarization plays out during binary BH mergers. As in our previous paper, we work in the decoupling approximation, i.e., we evolve the scalar field on a time-depenedent GR background. In Ref. [45], we studied a variety of possible processes for head-on BH collisions, as well as a quasicircular inspiral-merger of equal mass nonspinning binaries using a positive sign of the scalar-field-GB coupling. We demonstrated the existence of a process we coined *dynamical descalarization*, whereby initially scalarized BHs merged to form a larger remnant that descalarized because its GB curvature was too small to sustain the scalar hair. The alternative, the dynamical scalarization of the remnant, was not possible because its larger mass (compared to the initial BHs' masses) inevitably leads to a smaller GB curvature near the horizon.

However, for a negative sign of the coupling, the scalar field instability happens only for sufficiently rapidly spinning BHs ("spin-induced scalarization") [73–77]. This leads to the following questions:

(1) Does the formation of a highly spinning remnant cause spin-induced dynamical scalarization? If so, at what stage in the binary's evolution is the scalar hair excited?
(2) Can the process of dynamical descalarization found in Ref. [45] be generalized to the negative coupling case?

Here, we address these questions with a new suite of binary BH simulations and negative sign of the coupling constant.

We find that indeed spin-induced descalarization and scalarization of the BH remnant are both possible. The spin-induced descalarization of initially scalarized, spinning black holes (BHs), extends and completes the work in Ref. [45]. The spin-induced scalarization of the remnant is a new result. For values of the coupling constant close to the scalarization threshold, the growth of the scalar field has a large instability timescale. Therefore, scalarization only becomes significant significantly after the remnant BH's ringdown begins. We therefore now coin the term *stealth dynamical scalarization*, whereby the scalar field remains hidden throughout the full inspiral, merger and early ringdown evolution of the BH binary and is thus unconstrainable with GW observations.

In the remainder of this work, we explain how we arrived at these conclusions. In Sec. II, we review both scalarization and descalarization of BHs in sGB gravity. Next, in Sec. III, we discuss our numerical methods and our numerical relativity simulations designed to answer our previously stated questions. In Sec. IV, we present our findings and we finish by discussing some of their observational implications in Sec. V. We work with geometric units $G = 1 = c$.

II. SCALAR GAUSS-BONNET GRAVITY

A. Action and field equations

sGB gravity modifies GR via a nonminimal coupling between a real scalar field Φ and the GB invariant $\mathscr{G}$, as described by the action

$$S = \frac{1}{16\pi}\int \mathrm{d}^4x\sqrt{-g}\left[R - \frac{1}{2}(\nabla\Phi)^2 + \frac{\alpha_{\rm GB}}{4}f(\Phi)\mathscr{G}\right], \tag{1}$$

where R is the Ricci scalar, $g = \det(g_{\mu\nu})$ the metric determinant, $(\nabla\Phi)^2 = g^{\mu\nu}\nabla_\mu\Phi\nabla_\nu\Phi$ the scalar field kinetic term, and

$$\mathscr{G} = R^2 - 4R_{\mu\nu}R^{\mu\nu} + R_{\mu\nu\rho\sigma}R^{\mu\nu\rho\sigma}, \tag{2}$$

is the GB invariant, where $R_{\mu\nu\rho\sigma}$ and $R_{\mu\nu}$ are the Riemann and Ricci tensor, respectively. The particular form of the theory is parametrized by the coupling function $f(\Phi)$ and the coupling constant $\alpha_{\rm GB}$ with units of [Length]^2.

As in our previous study [45], we work in the decoupling limit. That is, we neglect the backreaction of the scalar field onto the spacetime metric: the scalar field evolves on a dynamical, vacuum background spacetime of GR. The action (1) gives rise to the field equation for Φ

$$\Box\Phi = -\frac{1}{4}\alpha_{\rm GB}f'(\Phi)\mathscr{G}, \tag{3}$$

where a prime denotes a derivative with respect to Φ. Since, we work in the decoupling limit, the d'Alembertian and the GB invariant are those of the time-dependent GR background.

The choice of the coupling function $f(\Phi)$ determines specific sGB models. As we already alluded to in Sec. I, the models can be classified into two types depending on the properties of their BH solutions. We label models as *type I* if the derivative of the coupling function $f'(\Phi) \neq 0$. In this case, BH solutions always have scalar hair [53–67]. Examples of type I models include the dilatonic $f(\Phi) \propto \exp(\Phi)$ [54–57] and shift-symmetric $f(\Phi) \propto \Phi$ [58–60] coupling functions. We label models as type II if the derivative of the coupling function $f'(\Phi_0) = 0$, for some constant Φ_0. In this case, the theory admits the stationary vacuum BH solutions of GR, as proved by the no-hair theorem of [69], but also admits, when the theorem is violated, scalarized BHs. Examples include quadratic $f(\Phi) \propto \Phi^2$ [69] and Gaussian $f(\Phi) \propto \exp(\Phi^2)$ [68] coupling functions. Here, we consider type II models only.

B. Scalarization of isolated black holes

In the second type of sGB model the onset of scalarization is found by linearizing Eq. (3) around the background BH spacetime, i.e., $\Phi = \Phi_0 + \delta\Phi$, where Φ_0 is a constant. This results in the scalar-field evolution equation

$$(\Box - m_{\rm eff}^2)\delta\Phi = 0, \tag{4}$$

with an effective mass squared

$$m_{\rm eff}^2 := -\frac{1}{4}\alpha_{\rm GB} f''(\Phi_0)\mathscr{G}, \tag{5}$$

which can become tachyonically unstable; in other words, the BH can scalarize if $m_{\rm eff}^2 < 0$ [68,69]. This, however, is a necessary, but not sufficient condition for scalarization. The scalarization threshold can be calculated by finding a bound state solution, i.e., a time independent solution of Eq. (4) which is regular at the BH horizon and that vanishes at spatial infinity. By imposing these boundary conditions on $\delta\Phi$, the calculation of the scalarization threshold is reduced to a boundary value problem, with the dimensionless ratio between $\alpha_{\rm GB}$ and the BH's mass squared playing the role of the eigenvalue. The smallest eigenvalue provides the scalarization threshold for the "fundamental" (i.e., the nodeless solution) family of scalarized BHs, while the other eigenvalues determine the threshold for the formation of "excited states" (i.e., solutions with one or more nodes). We focus on the latter here. See Fig. 1 in Ref. [69] or Sec. 4.3 of Ref. [82] for further details. To be more concrete, here we consider a quadratic coupling function,

$$f(\Phi) = \Phi^2. \tag{6}$$

The coupling strength is determined by the dimensionless constant[1]

$$\beta = \alpha_{\rm GB}/\mathscr{M}^2, \tag{7}$$

where $\mathscr{M}$ is the characteristic mass of the system. The effective mass then becomes

$$m_{\rm eff}^2 = -\frac{1}{2}\beta\mathscr{M}^2\mathscr{G}. \tag{8}$$

If $\mathscr{G}$ is positive-definite in the BH exterior, then the instability can only happen for positive β. However, if $\mathscr{G}$ is negative, at least in some regions outside the horizon, then the instability can also be triggered with a negative β. For example, consider the Kerr metric, for which the GB invariant in Boyer-Lindquist coordinates $(t, \bar{r}, \theta, \varphi)$ is given by

$$\mathscr{G}_{\rm Kerr} = \frac{48m^2}{(\bar{r}^2+\sigma^2)^6}(\bar{r}^6 - 15\bar{r}^4\sigma^2 + 15\bar{r}^2\sigma^4 - \sigma^6), \tag{9}$$

where $\sigma = a\cos\theta$ and $a = J/m$ is the angular momentum per unit mass of the BH. When the dimensionless spin $\chi = a/m < 0.5$, $\mathscr{G}$ is positive everywhere outside the event horizon and so scalarization can only take place if β is positive. This also holds true in the limiting case of a Schwarzschild BH. However, for sufficiently rapidly rotating BHs (i.e., those with $\chi = a/m \geq 0.5$), the GB invariant can become negative in the exterior of the outer BH horizon in regions along the rotation axis [83]. Hence, spin can induce scalarization of BHs if β is negative and $\chi \geq 0.5$ [73–78] and suppress it if β is positive [71,72].

One may note that scalarized solutions in quadratic sGB gravity with a positive coupling constant, $\beta > 0$, are unstable to radial perturbations [84]. Although this is true, such BHs can be stabilized by including higher-order scalar terms in the coupling $f(\Phi)$ [85,86], through the addition of scalar field self-interactions while retaining the quadratic form of $f(\Phi)$ [70], or through the addition of a coupling of scalar field to the Ricci scalar [87,88]. Since, we are investigating the onset of scalarization, it is unnecessary to include such terms and so we focus only on the quadratic coupling case here.

C. Scalarization and descalarization in black hole binaries

What could be the consequences of scalarization in BH binaries? To answer this question, in Ref. [45] we performed the first numerical relativity simulations of both head-on collisions and quasicircular inspirals of BHs in quadratic sGB gravity with a positive coupling β. We identified a new effect, that we named *dynamical descalarization*, in which initially nonspinning scalarized BHs shed-off completely their scalar hair after the merger. This is a result of the comparatively weaker curvature generated near the horizon of the resulting larger remnant BH. Consequently, several possible dynamical processes were discovered for particular combinations of mass ratio and coupling strength, as illustrated in Fig. 1 of Ref. [45]. We can contrast this with similar simulations in type I theories in which the remnant BH always retains some scalar hair [41].

Here, we extend our previous work by considering negative coupling $\beta < 0$ values. For this case the spins of the initial and/or remnant BHs play a crucial role in the development of the scalar field of the system due the possibility of spin-induced scalarization. Specifically, the formation of negative GB regions close to merger causes the remnant to scalarize, a process that we call *spin-induced dynamical scalarization*. Additionally, we also demonstrate *spin-induced dynamical descalarization*—the spin analogue of the aforementioned dynamical descalarization mechanism—as high-spinning binary components merge

[1]With respect to the notation of Ref. [45], we are omitting the subscript "2" and fixing $\bar{\beta} = 1$.

to produce a lower spin remnant that cannot support the instability.

III. SIMULATING BINARY BLACK HOLES IN SGB GRAVITY—METHODS AND SETUP

A. Time evolution formulation

We investigate the dynamics of the sGB scalar field, determined by its equation of motion (3), and sourced by a binary BH background spacetime. We perform a series of time evolution simulations in $3+1$ dimensions by adopting standard numerical relativity techniques; see, e.g., Ref. [89]. That is, we foliate the four-dimensional spacetime into three-dimensional spatial hypersurfaces Σ_t, parametrized by a time parameter t, with an induced spatial metric γ_{ij}. We introduce the timelike vector n^μ that is orthonormal to the hypersurface. Then, the spacetime metric $g_{\mu\nu}$ can be decomposed as

$$\begin{aligned} ds^2 &= g_{\mu\nu}dx^\mu dx^\nu \\ &= -(\alpha^2-\beta^k\beta_k)dt^2+2\gamma_{ij}\beta^i dt dx^j+\gamma_{ij}dx^i dx^j, \end{aligned} \tag{10}$$

where α is the lapse function (not to be confused with the dimensional coupling constant $\alpha_{\rm GB}$) and β^i is the shift vector (not to be confused with the dimensionless coupling constant β). Finally, we introduce the extrinsic curvature $K_{ij}=-\frac{1}{2\alpha}(\partial_t-\mathcal{L}_\beta)\gamma_{ij}$, where $\mathcal{L}_\beta$ is the Lie-derivative along the shift vector β^i.

To simulate the background BH binary, we write Einstein's equations as a Cauchy problem and adopt the Baumgarte-Shapiro-Shibata-Nakamura (BSSN) formulation [90,91] together with the moving puncture gauge conditions [92,93]. We prepare initial data describing a quasi-circular binary of two spinning BHs with the Bowen-York approach [94,95].

To evolve the scalar field Φ in this time-dependent GR background, we write its field equation (3) as a set of time evolution equations. Therefore, we introduce the scalar field's momentum $K_\Phi=-\frac{1}{\alpha}(\partial_t-\mathcal{L}_\beta)\Phi$ and we apply the spacetime decomposition to Eq. (3). This procedure gives the equations

$$(\partial_t-\mathcal{L}_\beta)\Phi=-\alpha K_\Phi, \tag{11a}$$

$$\begin{aligned} (\partial_t-\mathcal{L}_\beta)K_\Phi &= -D^i\alpha D_i\Phi \\ &\quad -\alpha\left(D^iD_i\Phi-KK_\Phi+\frac{1}{4}\alpha_{\rm GB}f'\mathcal{G}\right), \end{aligned} \tag{11b}$$

where D_i, $\mathcal{G}$ and $K=\gamma^{ij}K_{ij}$ are the covariant derivative with respect to the induced metric, the four-dimensional GB invariant and the trace of the extrinsic curvature of the background spacetime.

We initialize the scalar field to represent multiple scalarized BHs. For simplicity, we neglect the scalar field's initial linear and angular momentum, because it relaxes to its equilibrium configuration within about $100M$ from the start of the evolution, i.e., within approximately one orbit [41,96]. Since the scalar field equation (3) is linear, we can superpose the static bound-state solution anchored around an isolated BH. For N BHs, we then have

$$\Phi|_{t=0}=\sum_{a=1}^{N}\Phi_{(a)}, \qquad K_\Phi|_{t=0}=0, \tag{12}$$

where the subscript (a) labels the ath BH. The bound state of the sGB scalar field around an isolated, nonspinning BH with a coupling of the form (6) was obtained numerically in Ref. [69]. We approximate this solution with the fit

$$\Phi_{(a)}|_{t=0}=\frac{m_{(a)}r_{(a)}}{\varrho_{(a)}^2}\left[c_1+c_2\frac{m_{(a)}r_{(a)}}{\varrho_{(a)}^2}+c_3\frac{(m_{(a)}r_{(a)})^2}{\varrho_{(a)}^4}\right], \tag{13}$$

where $\varrho_{(a)}=m_{(a)}+2r_{(a)}$, $r_{(a)}$ is field point distance from the location of the ath BH in quasi-isotropic radial coordinates of the background spacetime, $m_{(a)}$ is the mass of the ath BH, and $c_1=3.68375$, $c_2=4.97242$, $c_3=2.29938\times10^2$ are fitting constants, where we corrected a misprint in c_3 in Ref. [45].

B. Code description

We performed the simulations with CANUDA [97], our open-source numerical relativity code for fundamental physics [41,45,98,99]. CANUDA is fully compatible with the EINSTEIN TOOLKIT [100–102], a public numerical relativity software for computational astrophysics. The EINSTEIN TOOLKIT is based on the CACTUS computational toolkit [103,104] and uses the CARPET driver [105,106] to provide boxes-in-boxes adaptive mesh refinement (AMR) as well as MPI parallelization. To evolve the field equations we employ the method-of-lines. Spatial derivatives are typically realized by fourth-order finite differences (with sixth order also being available) and for the time integration we use a fourth-order Runge-Kutta scheme.

The background spacetime, consisting of two spinning BHs in a quasi-circular orbit, is initialized with the TWOPUNCTURES spectral code [107] that solves the constraint equations of GR with the Bowen-York approach [94,95]. We evolve Einstein's equations using CANUDA's modern version of the LEAN thorn [108] that implements the BSSN equations with the moving puncture gauge. The sGB scalar field evolution equations (11) and its initial data (13) are implemented in CANUDA's arrangement CANUDA_EdGB_dec. Details of the implementation are described in Refs. [41,45,62]. To analyze the numerical data, we compute the Newman-Penrose scalar Ψ_4 as a measure for gravitational radiation and we extract the gravitational and scalar field multipoles on spheres of constant extraction radius $r_{\rm ex}$ using the QuasiLocalMeasures thorn [109]. We find the BHs' apparent

TABLE I. Setup of the simulations of equal-mass, quasicircular BH binaries. We show the initial separation d/M, the initial dimensionless spins χ_1 and χ_2 of each binary component, the dimensionless spin χ_f of the remnant, and the dimensionless coupling constant β used in the simulations. For reference, we also show the critical values to scalarize the initial ($\beta_{c,1} = \beta_{c,2}$) or final ($\beta_{c,f}$) BHs, calculated using Eqs. (14) and (15). The last column summarizes the process that unfolds during the simulation. We use $\bar{s}$ and s to denote unscalarized and scalarized states, respectively, and the subscript $\uparrow$ ($\downarrow$) indicates spin aligned (anti-aligned) with the orbital angular momentum, which is assumed to be $\uparrow$. See Fig. 2 for additional details.

Run	d/M	χ_1	χ_2	χ_f	β	$\beta_{c,1}$	$\beta_{c,f}$	Process
Setup A	10	0	0	0.68	−14.30	…	−12.96	$\bar{s}+\bar{s}\to s_\uparrow$
Setup B	10	−0.6	−0.6	0.48	−11.00	−10.55	…	$s_\downarrow+s_\downarrow\to\bar{s}_\uparrow$

horizons and compute their properties with the AHFinderDirect thorn [110,111].

C. Setup of simulations

To investigate spin-induced dynamical scalarization or descalarization in binary BH mergers, we have performed a series of simulations of equal-mass, quasicircular inspirals for the negative coupling case, $\beta < 0$. The initial BHs have either zero spin or a spin (anti-)aligned with the orbital angular momentum.

To choose the values of the coupling constant β in our simulations, we used the numerical data found in Ref. [74] (cf. Appendix, Table I) to obtain a fitting formula that returns the value of β at the threshold for spin-induced scalarization as a function of the dimensionless spin χ; we will refer to this threshold value as the *critical value* of the dimensionless coupling constant. The critical value for the coupling constant satisfies the scaling

$$\beta_c(m/M,\chi) = (m/M)^2\beta_c(1,\chi), \tag{14}$$

where m is a place-holder for either the individual masses of the binary $m_{(a)}$ or the final remnant mass m_f, while $M = m_1 + m_2$ is the initial total mass of the binary.

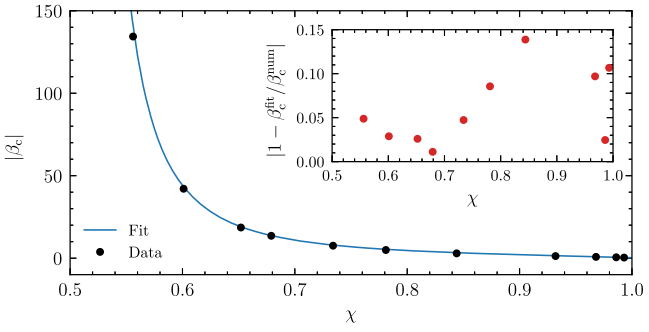

FIG. 1. Absolute value of the critical coupling, β_c, for spin-induced scalarization of a single BH as a function of the dimensionless spin χ. We show the numerical data of Ref. [74] and the fitting formula (15). The inset shows the relative error between the fit and the data. We see that the error is less than 15% in the range $0.5 \lesssim \chi < 1$ and less than 5% for $\chi \lesssim 0.74$.

The quantity $\beta_c(1,\chi)$ is the critical value of the coupling that leads to scalarization for a BH of mass $1M$ and dimensionless spin χ, namely

$$\beta_c(1,\chi) = -\frac{0.422}{(|\chi|-1/2)^2} + 1.487|\chi|^{7.551}, \tag{15}$$

where $\beta_c(1,\chi)$ diverges as $|\chi|$ tends to 0.5, in agreement with Ref. [76]. For instance, if we wish to scalarize the initial components of the binary, and if the mass ratio is unity, then $m_{(a)} = M/2$, and $\beta_{c,(a)}(1/2,\chi_{(a)}) = (1/4)\beta_c(1,\chi_{(a)})$. In Fig. 1, we show Eq. (15) and compare it against the numerical results of Ref. [74]. We obtain relative errors smaller than 15% in the range $0.5 \lesssim \chi < 1$ and less than 5% for $\chi \lesssim 0.74$. We use Eq. (14) as reference to choose the values of β to probe scalarization of either one (or both) of the initial binary components or of the remnant BH.

Here, we present two key simulations, listed in Table I and illustrated in Fig. 2, with the following setups:

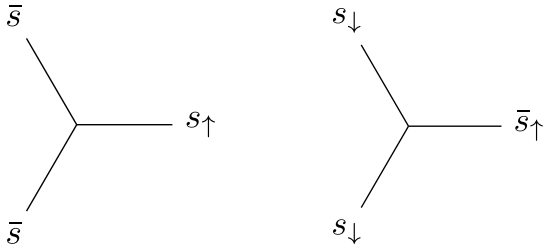

(a) Setup A (b) Setup B

FIG. 2. Binary BH simulations, where s ($\bar{s}$) stands for initial or final BH states that are scalarized (unscalarized) and with spin along the positive ($\uparrow$) or negative ($\downarrow$) z-direction (i.e., aligned or antialigned with the orbital angular momentum, assuming the latter is $\uparrow$). BH states without an arrow are nonspinning. Panel 2(a) illustrates a process of spin-induced dynamical scalarization: two initially unscalarized BHs produce a spinning, scalarized remnant. Panel 2(b) illustrates a process of dynamical descalarization: two initially rotating, scalarized BHs whose spin is antialigned with the orbital angular momentum merge into a rotating BH with a smaller spin magnitude. Consequently, the remnant descalarizes.

Setup A in Table I is designed to address our first question: does the formation of a highly spinning remnant cause spin-induced dynamical scalarization? Here, we consider a binary of initially nonspinning, unscalarized BHs that merges into a spinning, scalarized remnant as illustrated in Fig. 2(a). The BHs complete 10 orbits prior to their merger at $t_{\rm M} = 927M$, as estimated from the peak in the gravitational (quadrupole) waveform; see the bottom panel of Fig. 3. When the coupling β is negative, the squared effective mass (5) of the initial BHs (with $\chi = 0$) is positive definite everywhere outside their horizons, and so they are initially not scalarized. The final BH has a dimensionless spin of $\chi_f = 0.68$ and mass $m_f \sim M$. For a BH with these parameters, the critical coupling is $\beta_{{\rm c},f} \approx \beta_{\rm c}(1, 0.68) \approx -12.96$; cf. Eq. (14). In our simulation, we chose $|\beta| > |\beta_{{\rm c},f}|$ such that the remnant BH is indeed scalarized. In this simulation, we initialize the scalar field according to Eq. (13) around each binary component. The scalar field disperses early in the simulation, leaving each BH unscalarized and a negligible, but nonvanishing ambient scalar field in the numerical grid. Notice that if, we had set $\Phi|_{t=0} = 0$, there would be no scalar field dynamics [see Eq. (3)].

Setup B in Table I is designed to address our second question: is the dynamical descalarization found in Ref. [45] a general phenomenon? Is there a spin-induced dynamical descalarization? Here, we consider a binary of initially rotating, scalarized BHs with spins $\chi_1 = \chi_2 = -0.6$, anti-aligned with the orbital angular momentum as illustrated in Fig. 2(b). Each of the components of the binary has a mass $m_1 = m_2 = M/2$. Inserting these parameters in Eq. (14), we find $\beta_{{\rm c},1} = \beta_{{\rm c},2} = \beta_{\rm c}(1/2, -0.6) \approx -10.55$. In our simulations, we set $|\beta| \gtrsim |\beta_{\rm c}(1/2, -0.6)|$ such that the initial BHs are scalarized. The initial BHs merge into a final rotating BH that has a spin aligned with the orbital angular momentum of the previously inspiraling system, with a spin magnitude $\chi_f = 0.48$. This value is below the threshold for spin-induced scalarization, and so the remnant BH does not support scalar hair.

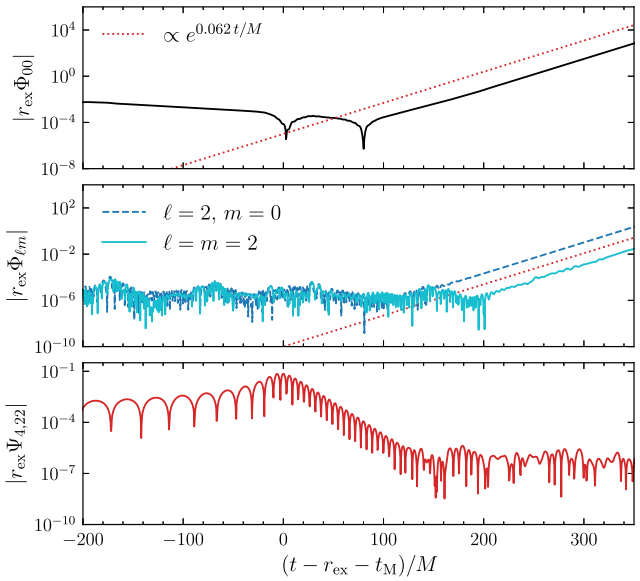

FIG. 3. Evolution of the scalar field monopole (top panel), scalar field $\ell = 2$ multipoles (middle panel) and the gravitational waveform of the background spacetime (bottom panel) for Setup A in Table I. We rescale the multipoles by the extraction radius $r_{\rm ex} = 100M$, and shift them in time such that $(t - r_{\rm ex} - t_{\rm M})/M = 0$ indicates the time of merger, determined by the peak of the gravitational waveform.

To show that our qualitative results are robust for a large variety of BH spin parameters, we have performed a series of additional simulations listed in Table II of Appendix A. All simulations presented in Tables I and II have the same grid setup: the numerical domain was composed of a Cartesian box-in-box AMR grid structure with seven refinement levels. The outer boundary was located at $255.5M$. We use a grid spacing of $dx = 0.7M$ on the outermost refinement level to ensure a sufficiently high resolution in the wave zone. The region around the BHs has a resolution of $dx = 0.011M$. To validate our code and estimate the numerical error of our simulations, we performed convergence tests for our most demanding simulation with $\chi_{1,2} = -0.6$, corresponding to Setup B in Table I. The relative error in the gravitational quadrupole waveform is $\Delta\Psi_{4,22}/\Psi_{4,22} \leq 0.8\%$, while the relative error of the scalar charge accumulates to $\Delta\Phi_{00}/\Phi_{00} \leq 30\%$ in the last orbits before merger; the latter is $\Delta\Phi_{00}/\Phi_{00} \leq 15\%$ in the merger and ringdown phase. The large error in the scalar field, close to the BHs merger, is a consequence of the exponential growth of the scalar field during inspiral. As our investigation is of a qualitative nature, this cumulative error is not a cause of concern for our results. However, a future quantitative analysis would have to address this issue. See Appendix B for details.

IV. RESULTS

A. Spin-induced dynamical scalarization

Here, we present key results obtained with simulation Setup A (see Sec. III C), corresponding to Fig. 2(a). In particular, we show that an initially unscalarized BH binary can indeed form a hairy, rotating remnant.

This process is illustrated in the top panel of Fig. 3, where we present the time evolution of the scalar field's monopole charge, $r_{\rm ex}\Phi_{00}$, measured at $r_{\rm ex} = 100M$, and shifted in time such that $(t - r_{\rm ex} - t_{\rm M})/M = 0$ indicates the time of merger. The scalar field perturbation that is initially present in our simulations remains small during the entire inspiral. See, for instance, the amplitudes $r_{\rm ex}\Phi_{\ell m}$ at $(t - r_{\rm ex} - t_{\rm M})/M < 0$ which are of $\mathcal{O}(10^{-4})$ or $\mathcal{O}(10^{-6})$. Yet, we see an exponential growth of the scalar charge, $r_{\rm ex}\Phi_{00} \sim e^{\omega_{\rm I,00}t}$, that exceeds the background fluctuations, approximately $100M$ after the merger. We estimate the

growth rate (for our choice of β) to be $M\omega_{\mathrm{I},00} \sim 0.062$ by fitting to the numerical data. We show this with the dotted red line in the top and middle panels.

We find a similar behavior in the scalar field quadrupole, as shown in the middle panel of Fig. 3. That is, both the axisymmetric $(\ell, m) = (2, 0)$ and the $(\ell, m) = (2, 2)$ multipoles are excited and grow exponentially with a rate of $M\omega_{\mathrm{I}} \sim 0.062$. For the form of the coupling function considered here, the rate appears to be independent of the (ℓ, m) multipole and is determined by the coupling constant β, as we further discuss later. The quadrupole scalar field is absent in the initial data because we initialized the scalar field with a spherically symmetric distribution around each of the BHs. Hence, the scalar field quadrupole we observe is caused by the "stirring" of the ambient scalar field due to the dynamical binary BH spacetime, which has a quadrupole moment. These Φ_{2m} multipoles also become unstable eventually, but at a later time relative to the monopole, as is evident by comparing the top and middle panels of Fig. 3. The exponential growth of the Φ_{2m} multipoles is consistent with the findings in Refs. [73,77], showing that higher-ℓ and $m \neq 0$ scalar field multipoles can also become unstable.

All of these results beg for the following questions: at what stage in the binary's evolution is the scalar field instability induced? Is it due to the orbital angular momentum at the late inspiral or is it due to the angular momentum of the remnant BH? As we discussed in Sec. II B, a necessary (but not sufficient) condition for the tachyonic instability to occur is for the GB invariant to become negative outside the BH horizon in the $\beta < 0$ case; see Eq. (8). To address these questions, we inspect the behavior of the GB invariant at different stages throughout the evolution.

In Fig. 4, we show a close-up of the GB invariant's (top panel) and the scalar field's (bottom panel) profiles along the z-axis, parallel to the orbital angular momentum, at different time snapshots throughout the evolution. In Fig. 5, we show the GB invariant $\mathcal{G}$ together with snapshots of the scalar field Φ in the xz-plane, perpendicular to the orbital plane of the binary. The snapshots correspond to time instants during the inspiral (top left), half an orbit before merger (top right), at the formation of the common apparent horizon (CAH) (bottom left) and about $200M$ after the merger (bottom right). The color map represents the scalar field amplitude and is shared among all panels, while the contours are isocurvature levels $|\mathcal{G}M^4| = \{1, 10^{-1}, 10^{-2}, 10^{-3}\}$, with positive (negative) values of $\mathcal{G}$ in black (red). We also show the location of the individual BHs using their apparent horizons, represented as ellipses with center, semimajor and semiminor axes given by the centroid, maximum and minimum radial directions as obtained with the AHFINDERDIRECT thorn [110,111]. We do not show the evolution of $\mathcal{G}$ in the equatorial plane because, we did not observe negative regions forming on this plane throughout the entire simulation.

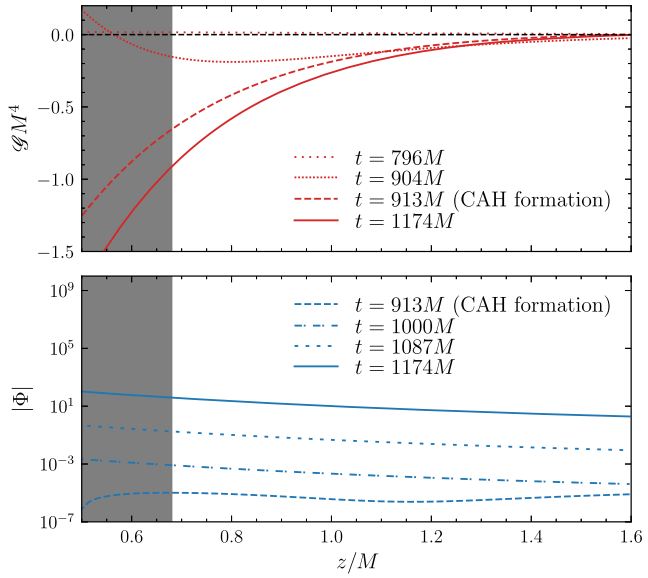

FIG. 4. Profiles of the GB invariant (top panel) and of the scalar field (bottom panel), corresponding to Setup A in Table I, along the z-axis in a close-up region near the CAH. The curves correspond to different times throughout the evolution. The shaded region indicates the CAH, shown $t = 100M$ after its formation when the final BH has relaxed to its stationary state. The GB invariant becomes negative during the BHs' last orbit before merger, and settles to its profile around the final rotating BH with dimensionless spin $\chi_f = 0.68$. In response, the scalar field becomes unstable.

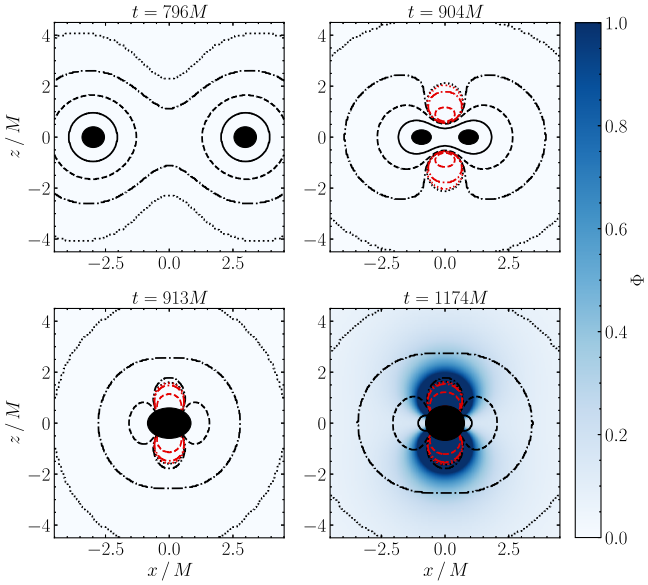

FIG. 5. Snapshots of the scalar field, Φ, and the GB invariant in the xz-plane corresponding to Setup A in Table I. The color map indicates the amplitude of the scalar field. The isocurvature contours of the GB invariant correspond to $|\mathcal{G}M^4| = 1$ (solid line), $|\mathcal{G}M^4| = 10^{-1}$ (dashed line), $|\mathcal{G}M^4| = 10^{-2}$ (dot-dashed line), $|\mathcal{G}M^4| = 10^{-3}$ (dotted line), black (red) lines correspond to positive (negative) values of $\mathcal{G}$. We show the inspiral (top left), half an orbit before merger (top right), formation of the first CAH (bottom left) and about $200M$ after the merger.

During the early inspiral, the GB invariant is positive around the individual, nonspinning BHs, and the scalar field remains small across the numerical grid as can be seen in the top left panel of Fig. 5. However, about half an orbit before merger, we see the formation of regions between the two BHs where the GB invariant is negative; see top right panel of Fig. 5 and top panel of Fig. 4, $t = 904M$ curve. By the time $t = 904M$, the effective mass squared defined in Eq. (8) has become negative and this, we re-emphasize, is a necessary, but not sufficient condition for the tachyonic instability to occur.

As the BHs merge and the system settles to a final, rotating BH, the GB invariant remains negative along the z-axis, which now coincides with the remnant BH's rotation axis. This is illustrated in the bottom panels of Fig. 5, which correspond to the instant of the formation of the CAH (bottom left) and to about $200M$ after the merger (bottom right). In response, the scalar field grows exponentially as can be seen in its profiles shown in the bottom panel of Fig. 4 for different times after the CAH has formed. The scalar field assumes a predominantly dipolar spatial distribution along the BH's spin axis, a consequence of the regions where the GB invariant is negative. We note that the scalar field continues to grow instead of settling to a stationary bound state because the magnitude of the coupling is larger than the critical value for spin-induced scalarization for the final BH with spin $\chi_f = 0.68$; see Table I.

To verify that the regions of negative GB curvature before the merger can induce the instability, we repeated the simulation of Setup A with a smaller initial BH separation of $d = 6M$ and a large-in-magnitude coupling constant $\beta = -10^3$; see Setup A1 in Table II. Although this choice of coupling, with $|\beta| \gg |\beta_{c,f}| = |\beta_c(1, 0.68)|$, may appear unphysical[2] it has the desired effect of being able to cause the instability before the merger and with a short timescale; both effects are controlled by $|\beta|$. This can be seen in Fig. 6, where we show the evolution of the scalar field multipoles, and in Fig. 7, where we show the field's profile along the rotation axis. Indeed, shortly after the GB invariant becomes negative, the scalar field grows exponentially and exceeds the magnitude of its background fluctuations at about $t = 20M$ before the CAH is first found.

In summary, if $|\beta|$ is large enough, the BHs' late inspiral and merger may be affected by the sGB scalar field. However, for $|\beta|$-values near the scalarization threshold,

[2]Such a large value of $|\beta|$ may be unphysical because the phase space of nonlinear BH solutions (i.e., including backreaction) has a band structure [69]: given a fixed value of M there is a maximum value of $|\beta|$ for which scalarized BHs exist. The domain of existence of scalarized BHs depends on $f(\Phi)$, the BH mass, and its spin. Thus, if this β is physical requires a careful, nonlinear analysis. Here, we focus only on the scalarization threshold.

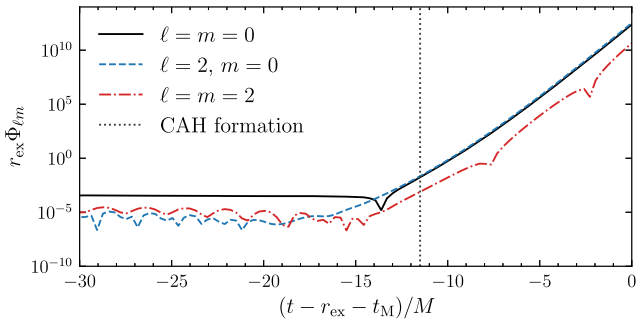

FIG. 6. Evolution of the $\ell = m = 0$ (solid line), $\ell = 2$, $m = 0$ (dashed line) and $\ell = m = 2$ (dot-dashed line) scalar field multipoles for the coupling $\beta = -10^3$; cf. Setup A1 in Table II. We rescale the multipoles by the extraction radius $r_{\rm ex} = 50M$ and shift them such that $(t - r_{\rm ex} - t_{\rm M})/M = 0$ indicates the time of merger determined by the peak in the gravitational waveform. For comparison, we also show the formation of the CAH (dotted line). We observe that the scalar field grows exponentially about $20M$ prior to the merger.

the inspiral and merger of initially unscalarized BH binaries, and their GW emission, are identical to that of GR and imprints of the sGB scalar field only appear during the late ringdown. Such effects may be very difficult (if not impossible) to detect, and this is what we refer to as *stealth scalarization*.

B. Spin-induced dynamical descalarization

In this section, we present our key results obtained with simulation Setup B in Table II (see Sec. III C), illustrated in Fig. 2(b). The setup corresponds to two initially rotating,

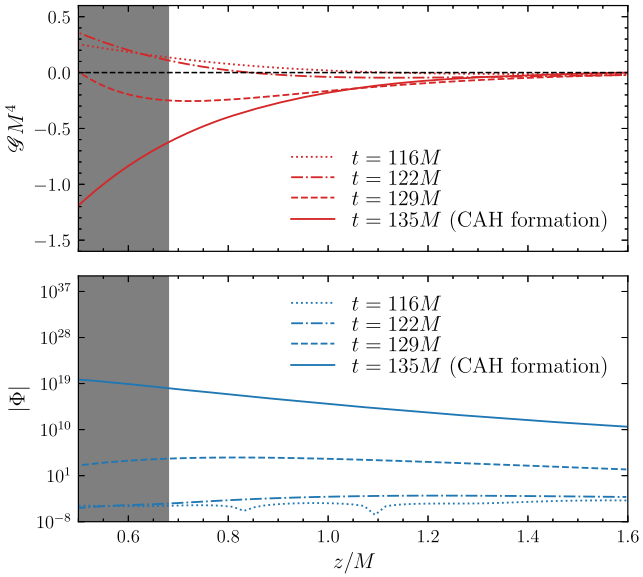

FIG. 7. Same as Fig. 4, but for Setup A1 in Table II. We see that the GB invariant (top panel) becomes negative and triggers the excitation of the scalar field (bottom panel) before the formation of the CAH, indicated by the gray region.

scalarized BHs (whose spin is antialigned with the orbital angular momentum) that produce a unscalarized remnant with a spin magnitude below the scalarization threshold for any choice of the coupling constant.

In Fig. 8, we show snapshots of the scalar field and the GB invariant in the xz-plane, perpendicular to the binary's orbital plane, during the inspiral (top left), half an orbit before the merger (top right), at the merger (bottom left) and about $t = 100M$ after the merger (bottom right). We illustrate the location of the BHs by their apparent horizons. The color-coding represents the amplitude of the scalar field and is shared among all panels. The contours represent the isocurvature lines $|\mathscr{G}M^4| = \{1, 10^{-1}, 10^{-2}, 10^{-3}\}$, with positive (negative) values shown in black (red). The spin magnitude of the two inspiraling BHs is sufficiently large to yield a GB invariant that has negative regions outside the BHs' horizon. Combined with our choice of $|\beta|$, the BHs sustain a scalar field bound state, as shown in the top left panel of Fig. 8 and the BHs carry a scalar "charge" during the inspiral. As the BHs merge, they form a single, rotating BH which has a spin aligned with the orbital angular momentum and a magnitude of $\chi_f = 0.48$. For this spin magnitude, the GB invariant is positive everywhere outside the BH's horizon, as shown in the bottom row of Fig. 8. As a consequence, the effective mass-squared becomes positive everywhere in the BH's exterior and the scalar field

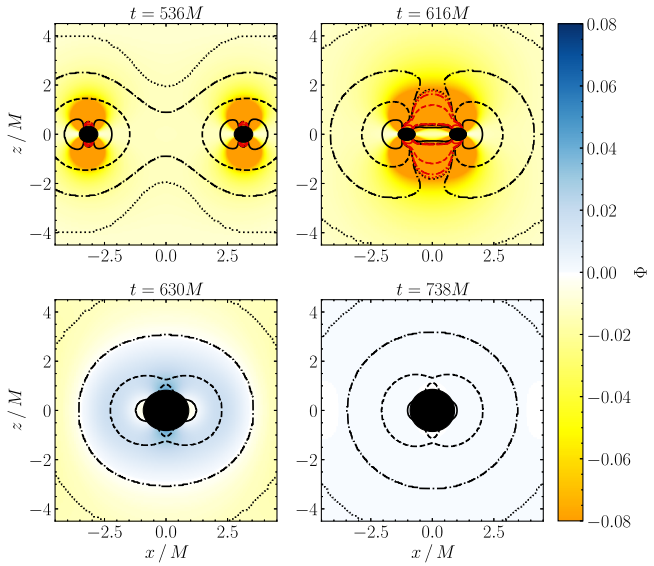

FIG. 8. Snapshots of the scalar field, Φ, and the GB invariant, $\mathscr{G}$, in the xz-plane, corresponding to Setup B in Table II. The color map represents the amplitude of the scalar field. The isocurvature contours indicate the magnitude of the GB invariant with $|\mathscr{G}M^4| = 1$ (solid line), $|\mathscr{G}M^4| = 10^{-1}$ (dashed line), $|\mathscr{G}M^4| = 10^{-2}$ (dot-dashed line), $|\mathscr{G}M^4| = 10^{-3}$ (dotted line), with positive (negative) values shown in black (red). We show the inspiral (top left), half an orbit before merger (top right), $10M$ after the CAH formation (bottom left) and about $100M$ after the merger (bottom right).

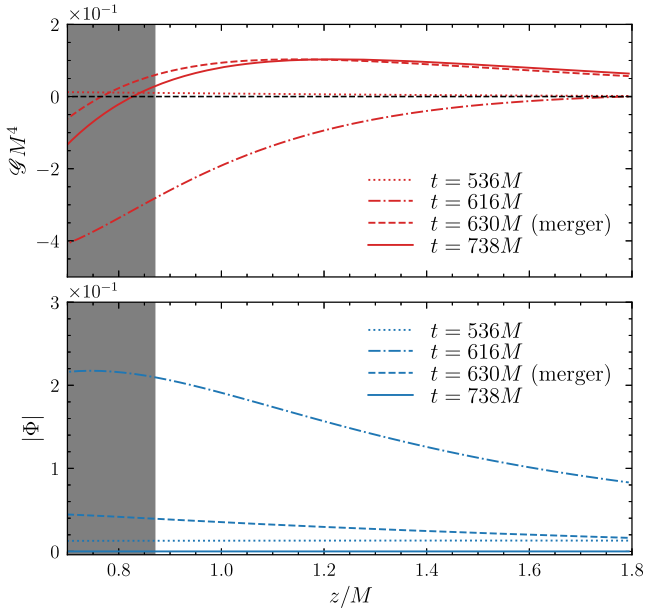

FIG. 9. Profiles of the GB invariant (top panel) and of the scalar field (bottom panel) for Setup B in Table II along the z-axis. The lines correspond to different times during the evolution. The shaded region indicates the CAH, shown $100M$ after its formation. The GB invariant becomes positive outside the horizon when the CAH is first formed. Consequently, the scalar field magnitude decreases and the remnant BH descalarizes.

bound states are no longer supported. That is, the scalar field dissipates, and the BH dynamically descalarizes, in agreement with the no-hair theorem of Ref. [69].[3]

These phenomena can also be seen in Fig. 9, where we show the profiles of the GB invariant (top panel) and of the scalar field (bottom panel) along the z-axis (parallel to orbital angular momentum) for several instants during the evolution. The shaded region indicates the apparent horizon of the final BH. The GB invariant remains negative outside the individual BHs during their (late) inspiral. Only when the CAH first forms, does the GB invariant become positive everywhere outside the remnant BH's horizon At this point, the effective mass-squared becomes positive, the tachyonic instability that kept each BH scalarized switches off, and the scalar field dissipates as shown in the bottom panel of Fig. 9.

[3]One might wonder if the final rotating BH may become superradiantly unstable due to the presence of an effective mass for the scalar field Φ. While the necessary conditions are satisfied [112–114], the instability for a BH of $\chi_f \lesssim 0.5$ would evolve on e-folding timescales much longer than those studied here [115,116]; see Ref. [73] for a comparison against spin-induced scalarization. Moreover, if backreaction of Φ onto the metric was included, the BH mass and spin would decrease until the superradiance condition is saturated and the instability is turned off. Then, the scalar decays and the end-state is a BH with no scalar field.

Does the presence of scalar charges during the inspiral produce scalar radiation? The answer is affirmative as can be seen in Fig. 10 where we show the time evolution of the scalar field monopole (top panel) and quadrupole (middle panel). For comparison, we also display the gravitational quadrupole waveform of the background spacetime (bottom panel). The scalar field monopole quantifies the development of the combined scalar charge of the BH binary measured on spheres of radius $r_{\rm ex} = 100M$, i.e., enclosing the entire binary. The total scalar charge remains approximately constant during the inspiral as the coupling is close to its critical value. Its magnitude increases about $10M$ before the merger which coincides with the formation of a joined region in which the GB invariant is negative due to the proximity of the two BHs As the BHs merge into a single rotating remnant with a spin below the threshold for the spin-induced scalarization, the scalar charge decays as illustrated in the inset of Fig. 10 (top panel). Because the scalar charges anchored around each BH follow the holes' orbital motion, they generate scalar radiation. In general, one would expect the scalar dipole to dominate the signal, as is also the case for shift-symmetric sGB gravity [37,38,41]. In the simulations shown here, however, the scalar dipole is suppressed due to the symmetry of the system (equal mass and spin of the companions), and the $\ell = m = 2$ multipole dominates.

The scalar waveform is displayed in the middle panel of Fig. 10 and shows the familiar chirp pattern: its amplitude and frequency increase as the scalar charges inspiral (following the inspiraling BHs in the background), and culminates in a peak as the BHs merge. The phase of the scalar field quadrupole clearly tracks its gravitational counterpart. Therefore, we deduce that the morphology (phase evolution) of the observed scalar quadrupole radiation is a result of the orbital dynamics of the system. A sufficiently large magnitude of the coupling constant may lead to an additional scalarization of the $\ell = 2$ mode, which would become manifest as an exponential growth of the signal superposed with the chirp. This situation is analogous to the evolutions with positive coupling shown in our previous work [45].

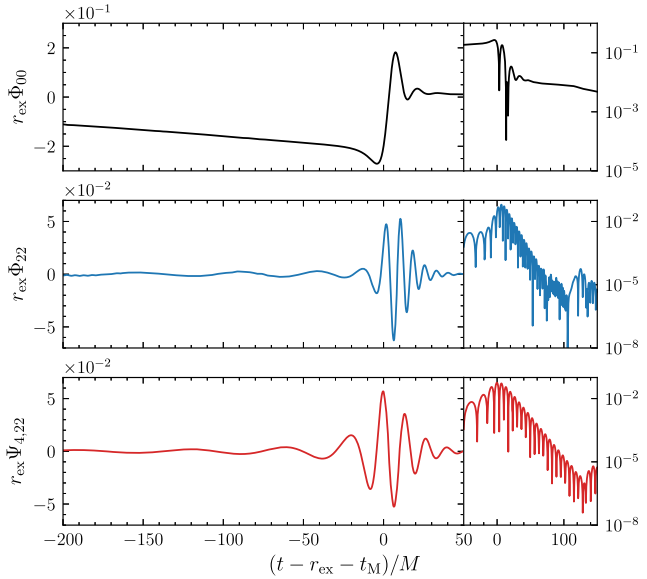

FIG. 10. Evolution of the scalar field monopole (top panel) and quadrupole (middle panel) and gravitational quadrupole (bottom panel) for Setup B in Table I. The waveforms are rescaled by the extractions radius $r_{\rm ex} = 100M$ and shifted in time such that $(t - r_{\rm ex} - t_{\rm M})/M = 0$ at the merger. In the insets we show the absolute values of the multipoles, in logarithmic scale, during the merger and ringdown.

After the merger, the scalar quadrupole exhibits a quasinormal ringdown pattern, i.e., an exponentially damped sinusoid, shown in the inset of Fig. 10 (middle panel). Here, in contrast to Ref. [45], descalarization occurs due to the vanishing of negative GB regions outside the remnant BH (because its final spin is $|\chi_f| < 0.5$), rather than due to a reduction of positive curvature (because of an increase in mass). We note that the scalar field rings down on similar timescales as the GW signal shown in the bottom panel of Fig. 10 for comparison. Therefore, one might expect a modification to the GW ringdown if backreaction onto the spacetime is included.

V. DISCUSSION

In this paper, we continued our study of dynamical scalarization and descalarization in binary BH mergers in sGB gravity by extending our previous work [45]. The latter focused on a positive coupling constant between the scalar field and the GB invariant, yielding dynamical descalarization in binary BH mergers. As a natural continuation, here we studied a negative coupling for which the BHs' spins play a major role in determining the onset of scalarization. In particular, we have shown that the merger remnant can either dynamically scalarize or dynamically descalarize depending on its spin and mass.

Spin-induced dynamical scalarization occurs when the merger remnant grows a scalar charge during coalescence due to the large spin of the remnant. In cases like this, the initial binary components lack a charge because their spins are not large enough to support one [73–78]. However, after the objects merge, the remnant BH spins faster than either component, allowing for a charge to grow. We found that it is possible for the scalar charge to grow as early as 1–2 orbits before a CAH has formed if the coupling $|\beta|$ is extremely large. This occurs because there are spacetime regions before merger (and near the poles of the future remnant) with a negative GB invariant, and a sufficient large value of $|\beta|$ allows bound states to form fast enough. We also found that if the coupling $|\beta|$ is close to the threshold, then scalarization occurs only in the late ringdown, because of the timescale required for the bound states to form.

Is such spin-induced scalarization detectable with current or future GW observatories? For values of $|\beta|$ near the scalarization threshold the instability timescale is large and the effects of the scalar field growth would only appear at

times much later than the merger and, more importantly, after the start of the ringdown. Hence, the inspiral-merger-ringdown of such a binary would be indistinguishable from one in GR, and scalarization would be a hidden or "stealth" effect, i.e., the remnant BH would acquire a charge, but its formation would not lead to an easily measurable effect. For instance, during the GW ringdown, which is dominated by the fundamental $(\ell, m) = (2, 2)$ quasinormal mode (QNM) frequency, we know that at a spin of $\chi \approx 0.68$, the decay time is approximately $\tau \approx 12.3M$ [117]. Hence, after $100M$ from the peak in the waveform, the dominant mode has decayed by roughly $\exp(-t/\tau) \approx \exp(-100/12.3) \approx 10^{-4}$. If the dominant QNM frequency begins to be modified only after $100M$, the GW has decayed so much that detecting this change or constraining it would be essentially impossible.

Is there no hope to detect such late times scalarization? Not necessarily. If we were to include the scalar field backreaction onto the spacetime, one could entertain the possibility that the late time growth of the scalar field (in particular of Φ_{22}) and the subsequent readjustment of the spinning remnant BH to its scalarized counterpart could result in a *second* GW signal. Confirming this possibility and, if confirmed, characterizing such a GW signal is left for future work.

Spin-induced dynamical descalarization occurs when the merger remnant loses its scalar charge during coalescence due to the low spin of the remnant. In cases like this, the initial binary components are spinning fast enough that each of them has a scalar charge and the remnant descalarizes if it has spin $\chi_f \leq 0.5$. Here, we demonstrated this effect in a example in which the initial binary components have their spin angular momenta antialigned with the orbital angular momentum. The merger produces a remnant BH with $\chi_f = 0.48$, for which no scalar field bound states are supported and the field is radiated away shortly ($\sim 10M$) after the CAH formation.

Is such spin-induced descalarization detectable with current or future GW observatories? For such descalarization to be detectable, one must first detect that the binary components were scalarized during the inspiral. Our simulations showed that the scalar charges lead to scalar quadrupole radiation because of the highly symmetric configurations (equal mass, equal spin magnitude) we chose to evolve. More realistic astrophysical configurations (with unequal masses and unequal spin magnitudes) forces the binary to emit scalar dipole radiation. Such emission of dipole or quadrupole radiation accelerates the inspiral, and thus affect the GW phase at -1PN and 0PN respectively, as shown in shift-symmetric theories [34–39]. These effects in the inspiral are observable and can thus be constrained with current ground-based [8,22–25] and future detectors [118,119] within the parametrized post-Einsteinian framework [120–123], provided the binary is of sufficiently low mass such that enough of the inspiral is observed [119]. In fact, a constraint of this type was recently obtained using the GW190814 event [124] in [21].

Let us then assume, for the sake of argument, that some future event reveals a scalar charge in the inspiraling binary components. Our results then indicate that descalarization may be detectable, if there is enough signal-to-noise ratio in the merger and ringdown [41,42]. This is because this process occurs at the same time and with the same timescales as the GW merger and ringdown, see Fig. 10. Future work could study the backreaction of the scalar field onto the metric to determine the magnitude of these modifications in the transient phase, without which one cannot assess detectability confidently. Our results indicate that descalarization might be best probed with a full inspiral-merger-ringdown analysis of the GW signal.

ACKNOWLEDGMENTS

We thank A. Cárdenas-Avendaño, A. Dima, and R. Teixeira da Costa for useful discussions. H. W. acknowledges financial support provided by NSF Grants No. OAC-2004879 and No. PHY-2110416, and Royal Society (UK) Research Grant No. RGF\R1\180073. N. Y. acknowledges support from the Simons Foundation through Grant No. 896696. M.E acknowledges support from the Science and Technology Facilities Council (STFC). This work made use of several computing infrastructures: the Extreme Science and Engineering Discovery Environment (XSEDE) Expanse through the allocation TG-PHY210114, which is supported by NSF Grant No. ACI-1548562; the Blue Waters sustained-petascale computing project which was supported by NSF Grant No. OCI-0725070 and No. ACI-1238993, the State of Illinois and the National Geospatial Intelligence Agency (Blue Waters is a joint effort of the University of Illinois at Urbana-Champaign and its National Center for Supercomputing Applications); the Illinois Campus Cluster, a computing resource that is operated by the Illinois Campus Cluster Program (ICCP) in conjunction with the National Center for Supercomputing Applications (NCSA) and which is supported by funds from the University of Illinois at Urbana-Champaign; the MINERVA cluster at the Max Planck Institute for Gravitational Physics; the Leibnitz Supercomputing Centre SuperMUC-NG under PRACE Grant No. 2018194669; the Jülich Supercomputing Center JUWELS HPC under PRACE Grant No. 2020225359; COSMA7 in Durham and Leicester DiAL HPC under DiRAC RAC13 Grant No. ACTP238. Our simulations were performed with CANUDA [41,97,99] and the EINSTEIN TOOLKIT [100–102]. Some of our calculations were performed with the *Mathematica* packages xPert [125] and INVAR [126,127], part of the xAct/xTensor suite [128,129]. The figures in this work were produced with MATPLOTLIB [130], KUIBIT [131] and TikZ-Feynman [132].

APPENDIX A: FULL SUITE OF SIMULATIONS

We ran a larger series of simulations, listed in Table II, of equal-mass BH binaries with varying initial spin that show

TABLE II. List of our complete series of simulations. We denote the initial separation d/M with M being the total mass, χ_1 and χ_2 are the initial dimensionless spin parameters of each BH, and χ_f is the final dimensionless spin parameter of the remnant. We use $\bar{s}$ and s to denote unscalarized and scalarized states, respectively, and the subscript $\uparrow$ ($\downarrow$) indicates spin aligned (antialigned) with the orbital angular momentum. The coupling chosen for each simulation is given by β, whereas $\beta_{c,1}$ and $\beta_{c,f}$ denote the critical couplings for the component/remnant BHs respectively.

Setup	d/M	χ_1	χ_2	χ_f	β	$\beta_{c,1}$	$\beta_{c,f}$	Process
A	10	0	0	0.68	−14.30	…	−12.96	$\bar{s}+\bar{s}\to s_\uparrow$
A1	6	0	0	0.68	−1000	…	−12.96	$\bar{s}+\bar{s}\to s_\uparrow$
A2	10	0.6	0.6	0.85	−2.9	−10.55	−3.01	$\bar{s}_\uparrow+\bar{s}_\uparrow\to s_\uparrow$
A3	10	0.6	0.6	0.85	−12.0	−10.55	−3.01	$s_\uparrow+s_\uparrow\to s_\uparrow$
A4	10	0.0	0.6	0.77	−12.0	−10.55	−5.59	$\bar{s}+s_\uparrow\to s_\uparrow$
B	10	−0.6	−0.6	0.48	−11.50	−10.55	…	$s_\downarrow+s_\downarrow\to \bar{s}_\uparrow$
B2	10	0.4	−0.6	0.64	−12.0	−10.55	−21.50	$\bar{s}_\uparrow+s_\downarrow\to \bar{s}_\uparrow$

a qualitatively same behavior as the runs presented in the main text. In particular, we simulated a series of initially spinning, unscalarized black holes that formed a scalarized remnant with larger spin. We also list example simulations in which one or both initial BHs are scalarized and they merge into an unscalarized remnant.

APPENDIX B: VALIDATION TESTS

To validate our code, we performed a suite of convergence tests. We ran Setup B, our numerically most demanding setup, at a lower resolution of $\mathrm{d}x_{\mathrm{low}} = 0.8M$ and a higher resolution of $\mathrm{d}x_{\mathrm{high}} = 0.625M$. The runs in the main text use a medium resolution of $\mathrm{d}x_{\mathrm{med}} = 0.7M$. The grid setup is the same across all simulations, see Sec. III. We estimated the order of convergence n and its associated convergence factor Q_n,

$$Q_n = \frac{(\mathrm{d}x_{\mathrm{low}})^n - (\mathrm{d}x_{\mathrm{med}})^n}{(\mathrm{d}x_{\mathrm{med}})^n - (\mathrm{d}x_{\mathrm{high}})^n}. \tag{B1}$$

We computed the n and Q_n for the gravitational waveform, $\Psi_{4,22}$, of the background spacetime and for the scalar charge. We show the corresponding convergence plots in Fig. 11. For $\Psi_{4,22}$, we find fourth order convergence, and we estimate the numerical (truncation) error to be $\Psi_{4,22}/\Psi_{4,22} \leq 0.8\%$. For the scalar field charge, Φ_{00}, we also find fourth order convergence. performed a convergence test on its $\ell = m = 0$ multipole. We show our result in the right panel of Fig. 11.

We find a cumulative error $\Delta\Phi_{00}/\Phi_{00} \leq 30\%$ in the late inspiral. The numerical error in the merger and ringdown is $\Delta\Phi_{00}/\Phi_{00} \leq 15\%$. As we restrict this work to a qualitative

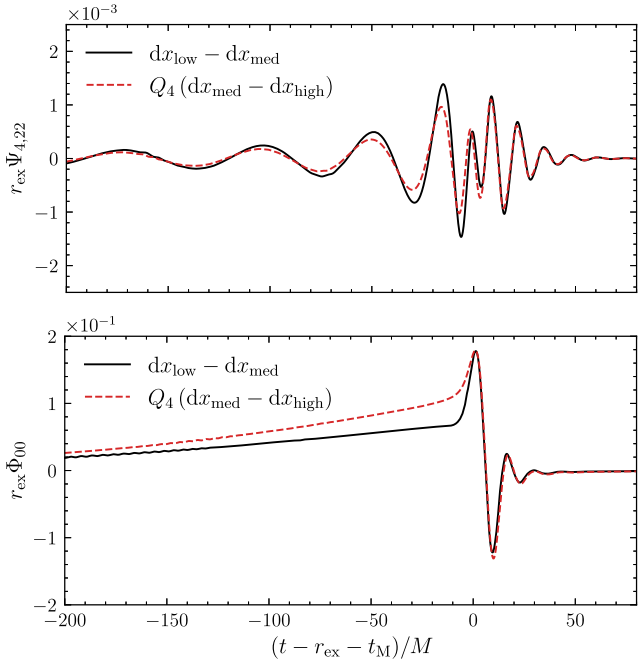

FIG. 11. Convergence plots for the $\ell = m = 2$ mode of the gravitational waveform (left panel) and the $\ell = m = 0$ mode of the scalar field (right panel). In both panels, we show the difference between the low and medium resolution run (solid line) and the medium and high resolution run (dashed line). The latter is rescaled by $Q_4 = 1.94$, indicating fourth order convergence. The lines are shifted in time such that $(t - r_{\mathrm{ex}} - t_{\mathrm{M}})/M = 0$ indicates the time of merger and they are rescaled by the extraction radius $r_{\mathrm{ex}} = 100M$.

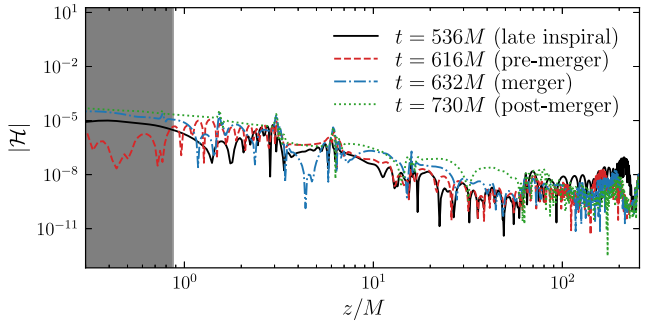

FIG. 12. Hamiltonian constraint along the z-axis during the late-inspiral (solid black), half an orbit before merger (dashed red), at the time of merger from the peak of the gravitational waveform (dash-dot blue) and $100M$ after merger (dotted green). The shaded region indicates the CAH, shown $100M$ after merger.

analysis, this error does not affect the main results of the paper. Further quantitative work, such as forecasting constraints on the theory would require this issue to be addressed.

Finally, in Fig. 12, we show the Hamiltonian constraint $\mathcal{H}$ along the z-axis for Setup B at different time instants. The constraint violation remains below 10^{-5} outside the BH horizon through the simulation.

[1] B. Abbott *et al.* (LIGO Scientific and Virgo Collaborations), GWTC-1: A Gravitational-Wave Transient Catalog of Compact Binary Mergers Observed by LIGO and Virgo during the First and Second Observing Runs, Phys. Rev. X **9**, 031040 (2019).

[2] R. Abbott *et al.* (LIGO Scientific and Virgo Collaborations), GWTC-2: Compact Binary Coalescences Observed by LIGO and Virgo During the First Half of the Third Observing Run, Phys. Rev. X **11**, 021053 (2021).

[3] R. Abbott *et al.* (LIGO Scientific, VIRGO, and KAGRA Collaborations), GWTC-3: Compact binary coalescences observed by LIGO and Virgo during the second part of the third observing run, arXiv:2111.03606.

[4] N. Yunes and X. Siemens, Gravitational-wave tests of general relativity with ground-based detectors and pulsar timing-arrays, Living Rev. Relativity **16**, 9 (2013).

[5] E. Berti *et al.*, Testing general relativity with present and future astrophysical observations, Classical Quantum Gravity **32**, 243001 (2015).

[6] E. Berti, K. Yagi, and N. Yunes, Extreme gravity tests with gravitational waves from compact binary coalescences: (I) Inspiral-merger, Gen. Relativ. Gravit. **50**, 46 (2018).

[7] E. Berti, K. Yagi, H. Yang, and N. Yunes, Extreme gravity tests with gravitational waves from compact binary coalescences: (II) Ringdown, Gen. Relativ. Gravit. **50**, 49 (2018).

[8] N. Yunes, K. Yagi, and F. Pretorius, Theoretical physics implications of the binary black-hole mergers GW150914 and GW151226, Phys. Rev. D **94**, 084002 (2016).

[9] B. P. Abbott *et al.* (LIGO Scientific and Virgo Collaborations), Tests of General Relativity with GW150914, Phys. Rev. Lett. **116**, 221101 (2016); **121**, 129902(E) (2018).

[10] B. P. Abbott *et al.* (LIGO Scientific and Virgo Collaborations), Tests of General Relativity with GW170817, Phys. Rev. Lett. **123**, 011102 (2019).

[11] B. Abbott *et al.* (LIGO Scientific and Virgo Collaborations), Tests of general relativity with the binary black hole signals from the LIGO-Virgo catalog GWTC-1, Phys. Rev. D **100**, 104036 (2019).

[12] A. Cardenas-Avendano, S. Nampalliwar, and N. Yunes, Gravitational-wave versus x-ray tests of strong-field gravity, Classical Quantum Gravity **37**, 135008 (2020).

[13] R. Abbott *et al.* (LIGO Scientific and Virgo Collaborations), Tests of general relativity with binary black holes from the second LIGO-Virgo gravitational-wave transient catalog, Phys. Rev. D **103**, 122002 (2021).

[14] H. O. Silva, A. M. Holgado, A. Cárdenas-Avendaño, and N. Yunes, Astrophysical and Theoretical Physics Implications from Multimessenger Neutron Star Observations, Phys. Rev. Lett. **126**, 181101 (2021).

[15] R. Abbott *et al.* (LIGO Scientific, VIRGO, and KAGRA Collaborations), Tests of general relativity with GWTC-3, arXiv:2112.06861.

[16] A. Ghosh, R. Brito, and A. Buonanno, Constraints on quasinormal-mode frequencies with LIGO-Virgo binary–black-hole observations, Phys. Rev. D **103**, 124041 (2021).

[17] G. Carullo, Enhancing modified gravity detection from gravitational-wave observations using the parametrized ringdown spin expansion coefficients formalism, Phys. Rev. D **103**, 124043 (2021).

[18] N. Sennett, R. Brito, A. Buonanno, V. Gorbenko, and L. Senatore, Gravitational-wave constraints on an effective field-theory extension of general relativity, Phys. Rev. D **102**, 044056 (2020).

[19] A. K. Mehta, A. Buonanno, R. Cotesta, A. Ghosh, N. Sennett, and J. Steinhoff, Tests of general relativity with gravitational-wave observations using a flexible-theory-independent method, arXiv:2203.13937.

[20] J. Zhao, L. Shao, Z. Cao, and B.-Q. Ma, Reduced-order surrogate models for scalar-tensor gravity in the strong field regime and applications to binary pulsars and GW170817, Phys. Rev. D **100**, 064034 (2019).

[21] L. K. Wong, C. A. R. Herdeiro, and E. Radu, Constraining spontaneous black hole scalarization in scalar-tensor-Gauss-Bonnet theories with current gravitational-wave data, Phys. Rev. D **106**, 024008 (2022).

[22] R. Nair, S. Perkins, H. O. Silva, and N. Yunes, Fundamental Physics Implications for Higher-Curvature Theories from Binary Black Hole Signals in the LIGO-Virgo Catalog GWTC-1, Phys. Rev. Lett. **123**, 191101 (2019).

[23] K. Yamada, T. Narikawa, and T. Tanaka, Testing massive-field modifications of gravity via gravitational waves, Prog. Theor. Exp. Phys. **2019**, 103E01 (2019).

[24] S. E. Perkins, R. Nair, H. O. Silva, and N. Yunes, Improved gravitational-wave constraints on higher-order curvature theories of gravity, Phys. Rev. D **104**, 024060 (2021).

[25] Z. Lyu, N. Jiang, and K. Yagi, Constraints on Einstein-dilaton-Gauss-Bonnet gravity from black hole-neutron star gravitational wave events, Phys. Rev. D **105**, 064001 (2022).

[26] H. O. Silva, A. Ghosh, and A. Buonanno, Black-hole ringdown as a probe of higher-curvature gravity theories, arXiv:2205.05132.

[27] K. Yagi, L. C. Stein, and N. Yunes, Challenging the presence of scalar charge and dipolar radiation in binary pulsars, Phys. Rev. D **93**, 024010 (2016).

[28] R. Metsaev and A. A. Tseytlin, Order α' (two loop) equivalence of the string equations of motion and the sigma model weyl invariance conditions: Dependence on the dilaton and the antisymmetric tensor, Nucl. Phys. **B293**, 385 (1987).
[29] P. Kanti and K. Tamvakis, Classical moduli $O(\alpha')$ hair, Phys. Rev. D **52**, 3506 (1995).
[30] P. A. Cano and A. Ruipérez, String gravity in $D = 4$, Phys. Rev. D **105**, 044022 (2022).
[31] C. Charmousis, From Lovelock to Horndeski's generalized scalar tensor theory, Lect. Notes Phys. **892**, 25 (2015).
[32] T. Kobayashi, M. Yamaguchi, and J. Yokoyama, Generalized G-inflation: Inflation with the most general second-order field equations, Prog. Theor. Phys. **126**, 511 (2011).
[33] T. Kobayashi, Horndeski theory and beyond: A review, Rep. Prog. Phys. **82**, 086901 (2019).
[34] K. Yagi, L. C. Stein, N. Yunes, and T. Tanaka, Post-newtonian, quasi-circular binary inspirals in quadratic modified gravity, Phys. Rev. D **85**, 064022 (2012); **93**, 029902(E) (2016).
[35] K. Yagi, N. Yunes, and T. Tanaka, Gravitational Waves from Quasi-Circular Black Hole Binaries in Dynamical Chern-Simons Gravity, Phys. Rev. Lett. **109**, 251105 (2012); **116**, 169902(E) (2016); **124**, 029901(E) (2020).
[36] K. Yagi, L. C. Stein, N. Yunes, and T. Tanaka, Isolated and binary neutron stars in dynamical Chern-Simons gravity, Phys. Rev. D **87**, 084058 (2013); **93**, 089909(E) (2016).
[37] B. Shiralilou, T. Hinderer, S. Nissanke, N. Ortiz, and H. Witek, Nonlinear curvature effects in gravitational waves from inspiralling black hole binaries, Phys. Rev. D **103**, L121503 (2021).
[38] B. Shiralilou, T. Hinderer, S. M. Nissanke, N. Ortiz, and H. Witek, Post-Newtonian gravitational and scalar waves in scalar-Gauss–Bonnet gravity, Classical Quantum Gravity **39**, 035002 (2022).
[39] F.-L. Julié and E. Berti, Post-Newtonian dynamics and black hole thermodynamics in Einstein-scalar-Gauss-Bonnet gravity, Phys. Rev. D **100**, 104061 (2019).
[40] F.-L. Julié, H. O. Silva, E. Berti, and N. Yunes, Black hole sensitivities in Einstein-scalar-Gauss-Bonnet gravity, Phys. Rev. D **105**, 124031 (2022).
[41] H. Witek, L. Gualtieri, P. Pani, and T. P. Sotiriou, Black holes and binary mergers in scalar Gauss-Bonnet gravity: Scalar field dynamics, Phys. Rev. D **99**, 064035 (2019).
[42] M. Okounkova, Numerical relativity simulation of GW150914 in Einstein dilaton Gauss-Bonnet gravity, Phys. Rev. D **102**, 084046 (2020).
[43] W. E. East and J. L. Ripley, Evolution of Einstein-scalar-Gauss-Bonnet gravity using a modified harmonic formulation, Phys. Rev. D **103**, 044040 (2021).
[44] W. E. East and J. L. Ripley, Dynamics of Spontaneous Black Hole Scalarization and Mergers in Einstein-Scalar-Gauss-Bonnet Gravity, Phys. Rev. Lett. **127**, 101102 (2021).
[45] H. O. Silva, H. Witek, M. Elley, and N. Yunes, Dynamical Descalarization in Binary Black Hole Mergers, Phys. Rev. Lett. **127**, 031101 (2021).
[46] D. D. Doneva, A. Vañó Viñuales, and S. S. Yazadjiev, Dynamical descalarization with a jump during black hole merger, arXiv:2204.05333.
[47] P. Pani and V. Cardoso, Are black holes in alternative theories serious astrophysical candidates? The Case for Einstein-Dilaton-Gauss-Bonnet black holes, Phys. Rev. D **79**, 084031 (2009).
[48] J. L. Blázquez-Salcedo, C. F. B. Macedo, V. Cardoso, V. Ferrari, L. Gualtieri, F. S. Khoo, J. Kunz, and P. Pani, Perturbed black holes in Einstein-dilaton-Gauss-Bonnet gravity: Stability, ringdown, and gravitational-wave emission, Phys. Rev. D **94**, 104024 (2016).
[49] J. L. Blázquez-Salcedo, D. D. Doneva, S. Kahlen, J. Kunz, P. Nedkova, and S. S. Yazadjiev, Axial perturbations of the scalarized Einstein-Gauss-Bonnet black holes, Phys. Rev. D **101**, 104006 (2020).
[50] J. L. Blázquez-Salcedo, D. D. Doneva, S. Kahlen, J. Kunz, P. Nedkova, and S. S. Yazadjiev, Polar quasinormal modes of the scalarized Einstein-Gauss-Bonnet black holes, Phys. Rev. D **102**, 024086 (2020).
[51] L. Pierini and L. Gualtieri, Quasi-normal modes of rotating black holes in Einstein-dilaton Gauss-Bonnet gravity: the first order in rotation, Phys. Rev. D **103**, 124017 (2021).
[52] A. Bryant, H. O. Silva, K. Yagi, and K. Glampedakis, Eikonal quasinormal modes of black holes beyond general relativity. III. Scalar Gauss-Bonnet gravity, Phys. Rev. D **104**, 044051 (2021).
[53] B. A. Campbell, N. Kaloper, and K. A. Olive, Classical hair for Kerr-Newman black holes in string gravity, Phys. Lett. B **285**, 199 (1992).
[54] S. Mignemi and N. Stewart, Charged black holes in effective string theory, Phys. Rev. D **47**, 5259 (1993).
[55] P. Kanti, N. Mavromatos, J. Rizos, K. Tamvakis, and E. Winstanley, Dilatonic black holes in higher curvature string gravity, Phys. Rev. D **54**, 5049 (1996).
[56] T. Torii, H. Yajima, and K.-i. Maeda, Dilatonic black holes with Gauss-Bonnet term, Phys. Rev. D **55**, 739 (1997).
[57] Z.-K. Guo, N. Ohta, and T. Torii, Black holes in the dilatonic Einstein-Gauss-Bonnet theory in various dimensions. I. Asymptotically flat black holes, Prog. Theor. Phys. **120**, 581 (2008).
[58] N. Yunes and L. C. Stein, Non-spinning black holes in alternative theories of gravity, Phys. Rev. D **83**, 104002 (2011).
[59] T. P. Sotiriou and S.-Y. Zhou, Black Hole Hair in Generalized Scalar-Tensor Gravity, Phys. Rev. Lett. **112**, 251102 (2014).
[60] T. P. Sotiriou and S.-Y. Zhou, Black hole hair in generalized scalar-tensor gravity: An explicit example, Phys. Rev. D **90**, 124063 (2014).
[61] R. Benkel, T. P. Sotiriou, and H. Witek, Dynamical scalar hair formation around a Schwarzschild black hole, Phys. Rev. D **94**, 121503 (2016).
[62] R. Benkel, T. P. Sotiriou, and H. Witek, Black hole hair formation in shift-symmetric generalised scalar-tensor gravity, Classical Quantum Gravity **34**, 064001 (2017).
[63] G. Antoniou, A. Bakopoulos, and P. Kanti, Evasion of No-Hair Theorems and Novel Black-Hole Solutions in Gauss-Bonnet Theories, Phys. Rev. Lett. **120**, 131102 (2018).
[64] G. Antoniou, A. Bakopoulos, and P. Kanti, Black-hole solutions with scalar hair in Einstein-scalar-Gauss-Bonnet theories, Phys. Rev. D **97**, 084037 (2018).

[65] K. Prabhu and L. C. Stein, Black hole scalar charge from a topological horizon integral in Einstein-dilaton-Gauss-Bonnet gravity, Phys. Rev. D **98**, 021503 (2018).
[66] M. Saravani and T. P. Sotiriou, Classification of shift-symmetric Horndeski theories and hairy black holes, Phys. Rev. D **99**, 124004 (2019).
[67] K. R. Abhishek Hegade, E. R. Most, J. Noronha, H. Witek, and N. Yunes, How do spherical black holes grow monopole hair?, Phys. Rev. D **105**, 064041 (2022).
[68] D. D. Doneva and S. S. Yazadjiev, New Gauss-Bonnet Black Holes with Curvature-Induced Scalarization in Extended Scalar-Tensor Theories, Phys. Rev. Lett. **120**, 131103 (2018).
[69] H. O. Silva, J. Sakstein, L. Gualtieri, T. P. Sotiriou, and E. Berti, Spontaneous Scalarization of Black Holes and Compact Stars from a Gauss-Bonnet Coupling, Phys. Rev. Lett. **120**, 131104 (2018).
[70] C. F. Macedo, J. Sakstein, E. Berti, L. Gualtieri, H. O. Silva, and T. P. Sotiriou, Self-interactions and spontaneous black hole scalarization, Phys. Rev. D **99**, 104041 (2019).
[71] P. V. Cunha, C. A. Herdeiro, and E. Radu, Spontaneously Scalarized Kerr Black Holes in Extended Scalar-Tensor–Gauss-Bonnet Gravity, Phys. Rev. Lett. **123**, 011101 (2019).
[72] L. G. Collodel, B. Kleihaus, J. Kunz, and E. Berti, Spinning and excited black holes in Einstein-scalar-Gauss–Bonnet theory, Classical Quantum Gravity **37**, 075018 (2020).
[73] A. Dima, E. Barausse, N. Franchini, and T. P. Sotiriou, Spin-Induced Black Hole Spontaneous Scalarization, Phys. Rev. Lett. **125**, 231101 (2020).
[74] C. A. R. Herdeiro, E. Radu, H. O. Silva, T. P. Sotiriou, and N. Yunes, Spin-Induced Scalarized Black Holes, Phys. Rev. Lett. **126**, 011103 (2021).
[75] E. Berti, L. G. Collodel, B. Kleihaus, and J. Kunz, Spin-Induced Black-Hole Scalarization in Einstein-Scalar-Gauss-Bonnet Theory, Phys. Rev. Lett. **126**, 011104 (2021).
[76] S. Hod, Onset of spontaneous scalarization in spinning Gauss-Bonnet black holes, Phys. Rev. D **102**, 084060 (2020).
[77] D. D. Doneva, L. G. Collodel, C. J. Krüger, and S. S. Yazadjiev, Black hole scalarization induced by the spin: $2+1$ time evolution, Phys. Rev. D **102**, 104027 (2020).
[78] S. Hod, Spin-induced black hole spontaneous scalarization: Analytic treatment in the large-coupling regime, Phys. Rev. D **105**, 024074 (2022).
[79] J. L. Ripley and F. Pretorius, Dynamics of a $\mathbb{Z}_2$ symmetric EdGB gravity in spherical symmetry, Classical Quantum Gravity **37**, 155003 (2020).
[80] T. Damour and G. Esposito-Farèse, Nonperturbative Strong Field Effects in Tensor-Scalar Theories of Gravitation, Phys. Rev. Lett. **70**, 2220 (1993).
[81] T. Damour and G. Esposito-Farèse, Tensor-scalar gravity and binary pulsar experiments, Phys. Rev. D **54**, 1474 (1996).
[82] H. O. Silva, C. F. B. Macedo, E. Berti, and L. C. B. Crispino, Slowly rotating anisotropic neutron stars in general relativity and scalar–tensor theory, Classical Quantum Gravity **32**, 145008 (2015).
[83] C. Cherubini, D. Bini, S. Capozziello, and R. Ruffini, Second order scalar invariants of the Riemann tensor: Applications to black hole space-times, Int. J. Mod. Phys. D **11**, 827 (2002).
[84] J. L. Blázquez-Salcedo, D. D. Doneva, J. Kunz, and S. S. Yazadjiev, Radial perturbations of the scalarized Einstein-Gauss-Bonnet black holes, Phys. Rev. D **98**, 084011 (2018).
[85] M. Minamitsuji and T. Ikeda, Scalarized black holes in the presence of the coupling to Gauss-Bonnet gravity, Phys. Rev. D **99**, 044017 (2019).
[86] H. O. Silva, C. F. Macedo, T. P. Sotiriou, L. Gualtieri, J. Sakstein, and E. Berti, Stability of scalarized black hole solutions in scalar-Gauss-Bonnet gravity, Phys. Rev. D **99**, 064011 (2019).
[87] G. Antoniou, A. Lehébel, G. Ventagli, and T. P. Sotiriou, Black hole scalarization with Gauss-Bonnet and Ricci scalar couplings, Phys. Rev. D **104**, 044002 (2021).
[88] G. Antoniou, C. F. B. Macedo, R. McManus, and T. P. Sotiriou, Stable spontaneously-scalarized black holes in generalized scalar-tensor theories, arXiv:2204.01684.
[89] M. Alcubierre, Introduction to $3+1$ Numerical Relativity, *International Series of Monographs on Physics* (Oxford University Press, Oxford, 2008).
[90] M. Shibata and T. Nakamura, Evolution of three-dimensional gravitational waves: Harmonic slicing case, Phys. Rev. D **52**, 5428 (1995).
[91] T. W. Baumgarte and S. L. Shapiro, On the numerical integration of Einstein's field equations, Phys. Rev. D **59**, 024007 (1998).
[92] M. Campanelli, C. Lousto, P. Marronetti, and Y. Zlochower, Accurate Evolutions of Orbiting Black-Hole Binaries Without Excision, Phys. Rev. Lett. **96**, 111101 (2006).
[93] J. G. Baker, J. Centrella, D.-I. Choi, M. Koppitz, and J. van Meter, Gravitational Wave Extraction from an Inspiraling Configuration of Merging Black Holes, Phys. Rev. Lett. **96**, 111102 (2006).
[94] J. M. Bowen and J. W. York, Jr., Time asymmetric initial data for black holes and black hole collisions, Phys. Rev. D **21**, 2047 (1980).
[95] S. Brandt and B. Bruegmann, A Simple Construction of Initial Data for Multiple Black Holes, Phys. Rev. Lett. **78**, 3606 (1997).
[96] H. Witek, L. Gualtieri, and P. Pani, Towards numerical relativity in scalar Gauss-Bonnet gravity: $3+1$ decomposition beyond the small-coupling limit, Phys. Rev. D **101**, 124055 (2020).
[97] H. Witek, M. Zilhao, G. Bozzola, M. Elley, G. Ficarra, T. Ikeda, N. Sanchis-Gual, and H. Silva, Canuda: A public numerical relativity library to probe fundamental physics (Zenodo, 2021), 10.5281/zenodo.5520862.
[98] H. Okawa, H. Witek, and V. Cardoso, Black holes and fundamental fields in numerical relativity: Initial data construction and evolution of bound states, Phys. Rev. D **89**, 104032 (2014).
[99] M. Zilhão, H. Witek, and V. Cardoso, Nonlinear interactions between black holes and Proca fields, Classical Quantum Gravity **32**, 234003 (2015).

[100] S. R. Brandt *et al.*, The Einstein toolkit (2021), to find out more, visit http://einsteintoolkit.org.
[101] F. Löffler *et al.*, The Einstein toolkit: A community computational infrastructure for relativistic astrophysics, Classical Quantum Gravity **29**, 115001 (2012).
[102] M. Zilhão and F. Löffler, An introduction to the Einstein toolkit, Int. J. Mod. Phys. A **28**, 1340014 (2013).
[103] T. Goodale, G. Allen, G. Lanfermann, J. Massó, T. Radke, E. Seidel, and J. Shalf, The Cactus framework and toolkit: Design and applications, in *Vector and Parallel Processing—VECPAR'2002, 5th International Conference, Lecture Notes in Computer Science* (Springer, Berlin, 2003).
[104] Cactus developers, Cactus Computational Toolkit, http://www.cactuscode.org/.
[105] E. Schnetter, S. H. Hawley, and I. Hawke, Evolutions in 3-D numerical relativity using fixed mesh refinement, Classical Quantum Gravity **21**, 1465 (2004).
[106] Carpet, Carpet: Adaptive Mesh Refinement for the Cactus Framework, https://bitbucket.org/eschnett/carpet.git.
[107] M. Ansorg, B. Brügmann, and W. Tichy, A single-domain spectral method for black hole puncture data, Phys. Rev. D **70**, 064011 (2004).
[108] U. Sperhake, Binary black-hole evolutions of excision and puncture data, Phys. Rev. D **76**, 104015 (2007).
[109] O. Dreyer, B. Krishnan, D. Shoemaker, and E. Schnetter, Introduction to isolated horizons in numerical relativity, Phys. Rev. D **67**, 024018 (2003).
[110] J. Thornburg, Finding apparent horizons in numerical relativity, Phys. Rev. D **54**, 4899 (1996).
[111] J. Thornburg, A fast apparent horizon finder for three-dimensional Cartesian grids in numerical relativity, Classical Quantum Gravity **21**, 743 (2004).
[112] Y. Shlapentokh-Rothman, Exponentially growing finite energy solutions for the Klein-Gordon equation on sub-extremal Kerr spacetimes, Commun. Math. Phys. **329**, 859 (2014).
[113] R. Brito, V. Cardoso, and P. Pani, Superradiance: New frontiers in black hole physics, Lect. Notes Phys. **906**, 1 (2015).
[114] G. Moschidis, Superradiant instabilities for short-range non-negative potentials on Kerr spacetimes and applications, arXiv:1608.02041.
[115] S. R. Dolan, Instability of the massive Klein-Gordon field on the Kerr spacetime, Phys. Rev. D **76**, 084001 (2007).
[116] S. R. Dolan, Superradiant instabilities of rotating black holes in the time domain, Phys. Rev. D **87**, 124026 (2013).
[117] E. Berti, V. Cardoso, and A. O. Starinets, Quasinormal modes of black holes and black branes, Classical Quantum Gravity **26**, 163001 (2009).
[118] Z. Carson, B. C. Seymour, and K. Yagi, Future prospects for probing scalar–tensor theories with gravitational waves from mixed binaries, Classical Quantum Gravity **37**, 065008 (2020).
[119] S. E. Perkins, N. Yunes, and E. Berti, Probing fundamental physics with gravitational waves: The next generation, Phys. Rev. D **103**, 044024 (2021).
[120] N. Yunes and F. Pretorius, Fundamental theoretical bias in gravitational wave astrophysics and the parameterized post-Einsteinian framework, Phys. Rev. D **80**, 122003 (2009).
[121] N. Cornish, L. Sampson, N. Yunes, and F. Pretorius, Gravitational wave tests of general relativity with the parameterized post-Einsteinian framework, Phys. Rev. D **84**, 062003 (2011).
[122] S. Tahura and K. Yagi, Parameterized post-Einsteinian gravitational waveforms in various modified theories of gravity, Phys. Rev. D **98**, 084042 (2018); **101**, 109902(E) (2020).
[123] S. Perkins and N. Yunes, Are parametrized tests of general relativity with gravitational waves robust to unknown higher post-Newtonian order effects?, Phys. Rev. D **105**, 124047 (2022).
[124] R. Abbott *et al.* (LIGO Scientific and Virgo Collaborations), GW190814: Gravitational Waves from the coalescence of a 23 solar mass black hole with a 2.6 solar mass compact object, Astrophys. J. Lett. **896**, L44 (2020).
[125] D. Brizuela, J. M. Martín-García, and G. A. Mena Marugan, xPert: Computer algebra for metric perturbation theory, Gen. Relativ. Gravit. **41**, 2415 (2009).
[126] J. M. Martín-García, R. Portugal, and L. R. U. Manssur, The invar tensor package, Comput. Phys. Commun. **177**, 640 (2007).
[127] J. M. Martín-García, D. Yllanes, and R. Portugal, The invar tensor package: Differential invariants of Riemann, Comput. Phys. Commun. **179**, 586 (2008).
[128] J. M. Martín-García, xPerm: Fast index canonicalization for tensor computer algebra, Comput. Phys. Commun. **179**, 597 (2008).
[129] xAct: Efficient tensor computer algebra for the Wolfram Language, http://www.xact.es/.
[130] J. D. Hunter, MATPLOTLIB: A 2D graphics environment, Comput. Sci. Eng. **9**, 90 (2007).
[131] G. Bozzola, KUIBIT: Analyzing Einstein Toolkit simulations with Python, J. Open Source Softwaare **6**, 3099 (2021).
[132] J. Ellis, TikZ-Feynman: Feynman diagrams with TikZ, Comput. Phys. Commun. **210**, 103 (2017).